

Robust quantum anomalous Hall effect in ferromagnetic transition metal halides

Chengxi Huang^{1,2,†}, Jian Zhou^{2,†,★} Haiping Wu¹, Kaiming Deng¹, Puru Jena^{2,★}, Erjun Kan^{1,★}

¹ *Department of Applied Physics and Key Laboratory of Soft Chemistry and Functional Materials (Ministry of Education), Nanjing University of Science and Technology, Nanjing, Jiangsu 210094, P. R. China*

² *Department of Physics, Virginia Commonwealth University, Richmond, Virginia 23284, United States*

† These two authors contributed equally to this work.

★Correspondence and requests for materials should be addressed to
J. Z. (jzhou2@vcu.edu), P. J. (pjena@vcu.edu), or E. K. (ekan@njust.edu.cn)

Abstract

The quantum anomalous Hall (QAH) effect is a novel topological spintronic phenomenon arising from inherent magnetization and spin-orbit coupling. Various theoretical and experimental efforts have been devoted in search of robust intrinsic QAH insulators. However, up to now, it has only been observed in Cr or V doped $(\text{Bi},\text{Sb})_2\text{Te}_3$ film in experiments with very low working temperature. Based on the successful synthesis of transition metal halides, we use first-principles calculations to predict that RuI_3 monolayer is an intrinsic ferromagnetic QAH insulator with a topologically nontrivial global band gap of 11 meV. This topologically nontrivial band gap at the Fermi level is due to its crystal symmetry, thus the QAH effect is robust. Its Curie temperature, estimated to be ~ 360 K using Monte-Carlo simulation, is above room temperature and higher than most of two-dimensional ferromagnetic thin films. We also discuss the manipulation of its exchange energy and nontrivial band gap by applying in-plane strain. Our work adds a new experimentally feasible member to the QAH insulator family, which is expected to have broad applications in nanoelectronics and spintronics.

Introduction

The discovery of topological insulators (TIs) is one of the most important developments in condensed matter physics during the last decade¹⁻³. With its bulk being semiconducting, the edge of a two-dimensional (2D) TI is metallic, showing quantum spin Hall conductivity, protected by time reversal symmetry. An interesting alternate topological quantum matter, quantum anomalous Hall (QAH) effect, arises when the time reversal symmetry is broken intrinsically, usually induced by internal magnetism⁴⁻⁶. This was first predicted by Haldane⁷. Subsequently, some 2D materials, such as transition metal (TM) doped TIs^{8,9}, TM decorated graphene¹⁰, TM based organometallic frameworks^{11,12}, and semi-functionalized stanene or germanene, are theoretically predicted to possess QAH effect^{13,14}. In these materials, the spin-orbit coupling (SOC) opens a global band gap at the Fermi level, resulting in topologically nontrivial insulating property. These QAH insulators are also referred to as Chern insulators, as their topological invariant Chern number is nonzero. In spite of being insulating in the bulk, the QAH insulators feature dissipation-less metallic chiral edge states with quantized conductivity, which makes them appealing for high efficiency quantum devices and spintronic applications.

Up to now, the QAH effect has only been experimentally observed in Cr or V doped $(\text{Bi},\text{Sb})_2\text{Te}_3$ thin film at very low operation temperature (< 85 mK), and the QAH conductance completely vanishes at 2 K¹⁴⁻¹⁶. For practical interests, one important challenge in synthesizing QAH insulators is to control the distribution of TM atoms, so that weakening of SOC by charge inhomogeneity can be diminished^{17,18}. In addition, the synthesis of such thin film is based on molecular beam epitaxy which is expensive and difficult to manipulate. Therefore, search and design of robust and experimentally feasible QAH insulators is important and still ongoing.

Recently, the experimentally synthesized TM^{III} halides^{19,20} have received much attention due to their potential applications in spintronics^{21,22}. Due to the weak interlayer

van der Waals interactions, these 3D layered crystals can be easily exfoliated down to 2D monolayers²²⁻²⁴, where the TM atoms are uniformly distributed in a honeycomb structure. This has motivated us to look for possible QAH insulators in this family. Although most TM^{III} halide monolayers are normal metal or semiconductors²³⁻²⁵, here we find that the ferromagnetic (FM) ruthenium halide (RuX_3 , X=Cl, Br, I) monolayers hold the possibility of being topologically nontrivial. Note that previous experimental and theoretical studies have shown that large halogen ligand or in-plane tensile strain can stabilize their FM coupling against antiferromagnetic (AFM) configuration^{23,24}. Besides, the SOC effect increases in heavier elements (proportional to Z^4). Hence, in the present work we use RuI_3 monolayer as an exemplary material to study their electronic and magnetic properties by using first-principles calculations. Our results reveal that the ground state of RuI_3 monolayer is FM with estimated Curie temperature T_c to be above the room temperature (~ 360 K). *Ab initio* molecular dynamics (AIMD) simulations confirm its thermal stability at 500 K. A clear Dirac cone in the spin down channel appears at the K point in the Brillouin zone near the Fermi level of its band structure, which is due to hybridization of ligand field induced spin down $\text{Ru-}e_1$ orbitals. We demonstrate that this Dirac cone is protected by the real space inversion symmetry of the Ru sublattice. After including SOC interactions, the Dirac cone opens a local band gap of 103 meV (at the K point), showing a topologically nontrivial feature. The system becomes an insulator with global band gap of 11 meV, in which QAH conductance appears. Thus, we predict that the RuI_3 monolayer is an intrinsic QAH insulator. This QAH effect is robust against any perturbation that keeps the crystal symmetry. In addition, we also discuss the strain effect on magnetic exchange energy and band gap of RuI_3 monolayer. The FM configurations of RuCl_3 and RuBr_3 monolayers are also discussed, where we find similar topologically nontrivial characters at the K point.

Results and discussion

Figure 1a shows the optimized structure of the RuI₃ monolayer which consists of three flat atomic layers, namely, top-I layer, middle-Ru layer, and bottom-I layer. The equilibrium lattice constant of hexagonal lattice is 7.10 Å which is larger than that of RuCl₃ monolayer, namely, 5.96 Å²⁶.⁽²⁶⁾ Each Ru atom is coordinated to six I atoms with Ru-I bond length of 2.71 Å. The geometric structure is crystallographically subject to the *P-31m* layer group (no. 71). The “thickness” of this monolayer, defined as the distance between the vertical coordinates of the top-I layer and the bottom-I layer, is 3.05 Å. We also calculate its formation energy $E_f = (E_{\text{RuI}_3} - 1/4\mu_{\text{Ru}} - 3/4\mu_{\text{I}})$, where E_{RuI_3} is the cohesive energy of RuI₃ monolayer. The chemical potential μ_{Ru} and μ_{I} are taken from the cohesive energy of hcp Ru crystal and I₂ molecule, respectively. The calculated formation energy of RuI₃ monolayer is -0.23 eV. This negative value is indicative of exothermic reaction. The thermal stability is examined by performing AIMD simulations up to 500 K in a (3×3×1) supercell (Fig. S1 in Supplementary Information). After 3,000 simulation time steps with each time step of 1 fs, we find slight distortions of the structure. The total potential energy fluctuates around a constant magnitude, implying that the exfoliation reaction to obtain RuI₃ monolayers can be carried out at high temperature.

Next, we explore the electronic and magnetic properties of RuI₃ monolayer. Since each I atom needs one electron from Ru (with its valence state of 4d⁷5s¹), the formal oxidation state of Ru is +3. There leave five *d* electrons on each Ru atom, thus the system is expected to be spin polarized. This is confirmed by our calculation which shows that each Ru atom carries $\sim 1 \mu_{\text{B}}$ magnetic moment. In order to determine the optimal magnetic coupling, we consider four possible magnetic configurations (one FM and three AFM) as shown in Fig. 1b. We find that the FM state has the lowest total energy (spin density shown in Fig. 1c). The relative energies between the FM and AFM states are listed in Table S1. During our calculation the Néel-AFM configuration always automatically converged to nonmagnetic state, whose total energy is higher than that of the FM state by

42 meV per formula unit (RuI_3 , denoted as f.u. thereafter). The zigzag-AFM and stripy-AFM states are energetically higher than that of the FM coupling by 20 and 36 meV/f.u., respectively. We found these results to remain qualitatively unchanged when GGA+ U method was applied (Table S2). These suggest a robust FM ground state of RuI_3 monolayer.

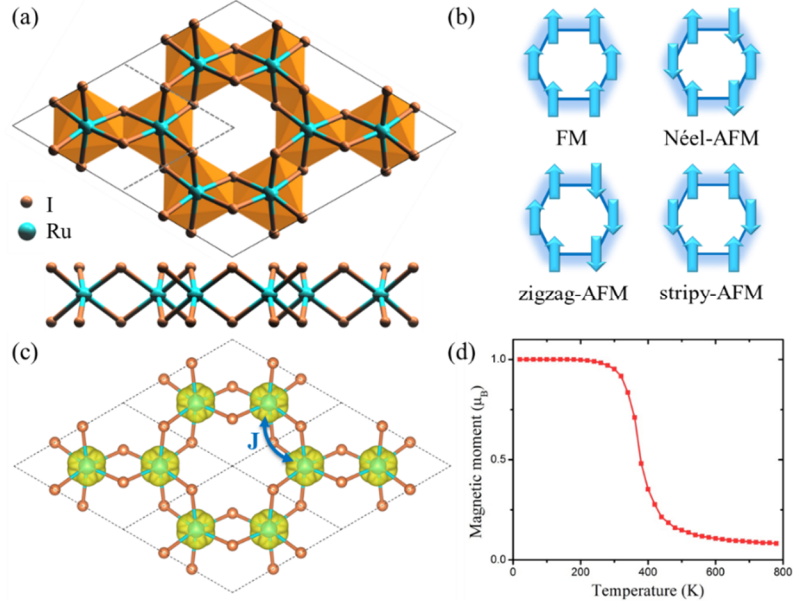


Figure 1. (a) Top and side view of the optimized 2D RuI_3 monolayer. Dashed rhombus refers to the primitive cell. (b) Possible magnetic configurations considered. (c) Spin density (iso-value of $0.04 \text{ e}/\text{\AA}^3$) and exchange path J . (d) Magnetic moment per formula unit as a function of temperature from Monte-Carlo simulation.

To examine the spin dynamical stability against temperature, we use Ising model to describe the spin Hamiltonian, i.e. $H = -\sum_{\langle ij \rangle} JS_i \cdot S_j$, where J refers to the nearest-neighbor exchange parameter (Fig. 1c), $S = \frac{1}{2}$ according to our calculation, and the summation runs over all nearest-neighbor Ru sites. Since the converged magnetic moment per Ru of zigzag-AFM state is most close to that of the FM state, we estimate the exchange parameter J using the energy difference between FM and zigzag-AFM state. The J is calculated to be 82 meV, with positive value indicating FM exchange coupling.

Next we perform Monte-Carlo simulations to estimate its Curie temperature (T_c). A (20×20) supercell is adopted to reduce translational constraint. The magnetic moment per f.u. is taken after the system reaches equilibrium state at a given temperature. In Fig. 1d, we see that T_c is ~ 360 K, which is above room temperature and higher than those of most 2D FM nanomaterials²⁷⁻²⁹.

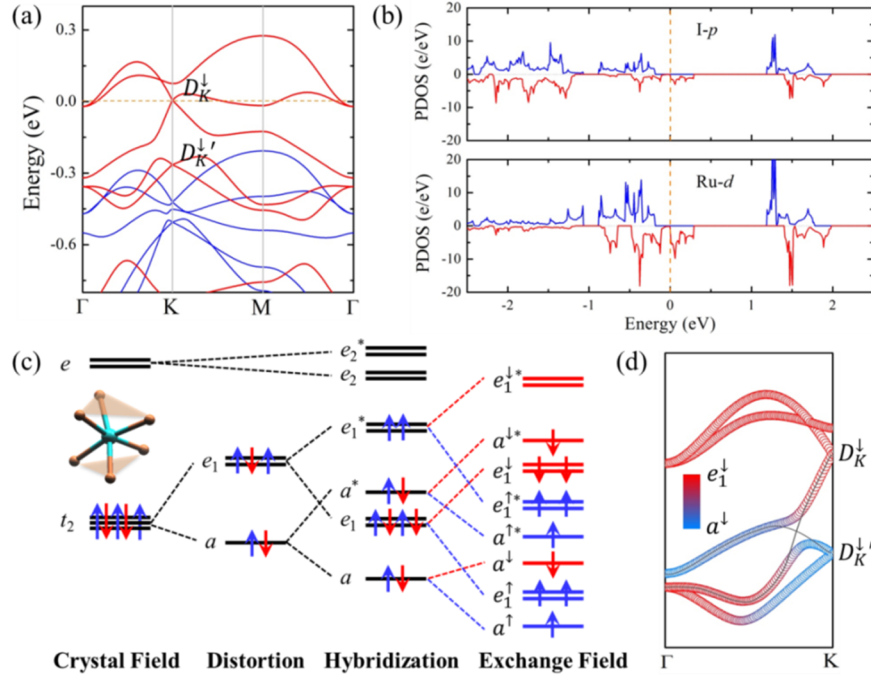


Figure 2. (a) Band structure without SOC. Blue and red curves represent spin up and spin down bands, respectively. The D_K^\downarrow and $D_K^{\downarrow'}$ denote two Dirac states at the K point. (b) Projected density of states. (c) Schematic diagram of the evolution from the atomic d orbitals to the final states at the Γ point. (d) Orbital-resolved spin-down bands around the Fermi level. Different colors represent proportional contribution of e_1^\downarrow states and a^\downarrow states (see the color bar inset). Thin black curves show the evolution of e_1^\downarrow and a^\downarrow states from Γ to K .

To gain insight into the electronic properties of FM RuI₃ monolayer we calculate the electronic band structure and projected density of states (PDOS). Figure 2a shows the spin-polarized band structure of the FM ground state without including SOC. We find

two Dirac cones at the K point in the spin down channel (red curves), denoted as D_{K^\downarrow} and $D_{K^\downarrow'}$. The D_{K^\downarrow} is located slightly above the Fermi level (E_F+5 meV with E_F the Fermi energy), and the $D_{K^\downarrow'}$ is below the Fermi level (E_F-265 meV). From the projected DOS (Fig. 2b), we see that both these Dirac cones are mainly contributed by Ru- d orbitals. In the spin up channel (blue curves), there are also two similar Dirac cones at the K point, but they are located much lower than the Fermi level due to large spin splitting.

To better understand the band structure, we start from the d orbitals of a Ru atom. Geometrically speaking, each Ru atom is coordinated by six I atoms, forming a distorted octahedral crystal field. In a perfect octahedral crystal field, the five d orbitals split into e and t_2 sub-states. In this distorted octahedral crystal field, the t_2 further splits into a and e . Hence, the five d orbitals split into three distinct sub-states, i.e. a , e_1 , and e_2 (little group at Γ point is D_{3d}). This is consistent with our calculated PDOS results. Due to strong ligand field effect, the five Ru^{3+} d electrons occupy only the a and e_1 orbitals, leaving the e_2 empty (distortion step in Fig. 2c). Furthermore, the hybridizations between two Ru- a and Ru- e_1 orbitals form bonding and antibonding states. In this way, a , e_1 , and, a^* orbitals are fully occupied by eight electrons (four spin up and four spin down), and the degenerate e_1^* states are half-filled by two spin up electrons, in keeping with the Hund's rule (hybridization step of Fig. 2c). Such half-filling also implies a stable electron configuration. The exchange between two e_1^* orbitals also explains the FM ground state with a magnetic moment of $2 \mu_B$ in one unit cell. After incorporating the magnetic exchange field, an energy split occurs between the spin up and spin down orbitals. Hence, the $a^{\downarrow*}$ and $e_1^{\downarrow*}$ lie higher in energy than the $e_1^{\uparrow*}$. This is consistent with the DFT calculated band alignments at the Γ point. Considering the honeycomb lattice of Ru atoms (which contains inversion symmetry of Ru sub-lattice), the e_1^\downarrow and $e_1^{\downarrow*}$ bands disperse in the momentum space and form Dirac point D_{K^\downarrow} at the K point. Similarly, the dispersion of a^\downarrow and $a^{\downarrow*}$ forms the $D_{K^\downarrow'}$ point. Thus, these Dirac points are protected by

crystal symmetry of the Ru sub-lattice, and are robust against perturbations (such as in-plane strains) which keep its symmetry.

Now, we turn on the SOC interaction. Figure 3a shows the band structure including SOC, where the degeneracy of D_K^\downarrow is lifted, opening a direct band gap of 103 meV at the K point and a global indirect band gap of 11 meV at the Fermi level. Similar band opening also occurs in the $D_{K'}^\downarrow$ point. Such band gap opening at the K point suggests a topologically nontrivial feature at the Fermi level. Note that, due to the SOC effect, the out-of-plane spin component s_z of valence band is slightly quenched. In order to identify its topological property, we calculate the Berry curvature (Ω) and Chern number (C) of each band by using the Kubo formula^{30,31},

$$C = \sum_{n \in \{O\}} C_n = \frac{1}{2\pi} \int \sum_{n \in \{O\}} \Omega_n(k) d^2k = \sum_{n \in \{O\}} (C_{n,\uparrow} + C_{n,\downarrow}),$$

$$\Omega(k) = \sum_{n \in \{O\}} \Omega_n(k) = -2 \sum_{n \in \{O\}} \sum_{n' \neq n} \frac{\text{Im} \langle \psi_{n,k} | v_x | \psi_{n',k} \rangle \langle \psi_{n',k} | v_y | \psi_{n,k} \rangle}{(E_{n,k} - E_{n',k})^2},$$

where n is the band index, $\psi_{n,k}$ is the eigenstate, $v_{x,y}$ is the velocity operator, and $\{O\}$ refers to occupied band set. The calculated Chern number of each frontier band is indicated in Fig. 3a. The k -resolved Berry curvature is shown in Fig. 3b. One clearly sees pronounced positive peaks located at the K points. Hence, the integration of Berry curvatures for all occupied bands yields a nonzero Chern number $C = -1$, indicating a quantized Hall conductance $\sigma_{xy} = C \cdot e^2/h$ within the bulk band gap. Thus, we demonstrate that the RuI₃ monolayer is a QAH insulator. To be specific, we adjust the chemical potential (relative to the Fermi level) and calculate the anomalous Hall conductance variation, as shown in the right panel of Fig. 3a. We find a quantized platform of σ_{xy} ($-1 \times e^2/h$) within the energy window of the global band gap (11 meV); σ_{xy} gradually decreases when the chemical potential is shifted out of the band gap. Note that the σ_{xy} remains nonzero when the chemical potential lies between -0.1 and $+0.2$ eV relative to E_F . This large range of nonzero σ_{xy} is different from previous studies where σ_{xy} decreases

to zero rapidly out of the energy gap^{10,12,32,33}. This would enhance the possibility to observe anomalous Hall conductance in experiments.

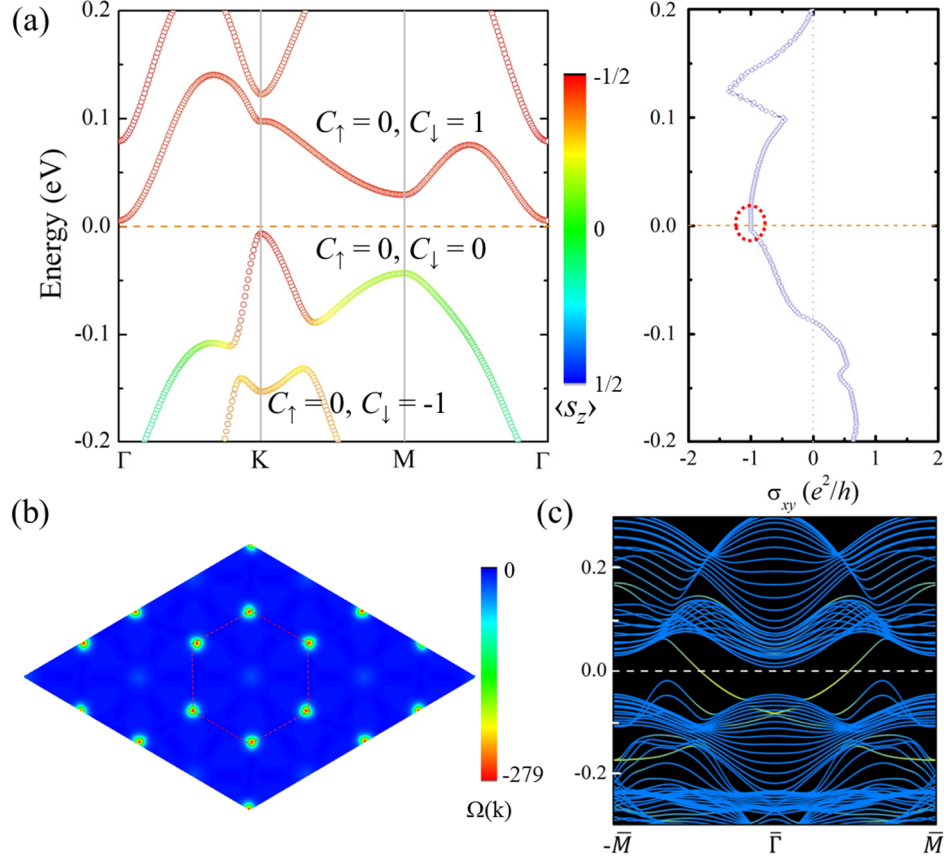


Figure 3. (a) Band structure with SOC (left panel) and anomalous Hall conductance as a function of relative chemical potential (right panel). Different colors in the band structure represent the $\langle s_z \rangle$. The Chern numbers of frontier bands are indicated. The quantized terrace of σ_{xy} is highlighted by the red dashed oval. (b) k -resolved Berry curvature $\Omega(k)$. Red dashed hexagon denotes the first Brillouin zone. (c) TB band structure of nanoribbon obtained by MLWFs show edge states (yellow) inside the gap of bulk bands (blue).

One can also confirm the QAH effect by calculating its chiral edge state within the nontrivial band gap. We fit a tight-binding (TB) Hamiltonian by using maximally localized Wannier functions (MLWFs)³⁴ to the DFT calculated bands, as implemented in

the Wannier90 package³⁵. As shown in Fig. S2, they show very good agreement around the Fermi energy. Without loss of generality, we build a zigzag edged nanoribbon and calculate its band structure using the TB Hamiltonian (Fig. 3c). One clearly sees a metallic edge state appearing in the $\bar{\Gamma} \rightarrow \bar{M}$ path (the metallic state in the $-\bar{M} \rightarrow \bar{\Gamma}$ path corresponds to the opposite edge of the nanoribbon). Since the Chern number C equals to the number of metallic edge states cutting the Fermi level, here we demonstrate that $|C| = 1$.

Another important physical property that a QAH insulator possesses is its optical Hall conductivity in the ac regime, which can be measured through the magneto-optical experiment. Using Kubo formula the optical Hall conductivity can be written as

$$\sigma_{ac}(\omega) = \frac{e^2}{h} \int \frac{d^2k}{2\pi} \sum_{n' \neq n} (f_{n,k} - f_{n',k}) \frac{\text{Im} \langle \psi_{n,k} | v_x | \psi_{n',k} \rangle \langle \psi_{n',k} | v_y | \psi_{n,k} \rangle}{(\omega_{n',k} - \omega_{n,k}) - (\omega + i\eta)},$$

where $f_{n,k}$ is Fermi-Dirac distribution, ω is incident optical frequency, and η is an infinitesimal parameter. By tuning the chemical potential, we plot the real and imaginary parts of σ_{ac} in Fig. 4, which reflect the reactive and dissipative behavior of an incident photon, respectively. We observe that σ_{ac} fluctuates when $0 < \hbar\omega < 0.5$ eV and $1.3 < \hbar\omega < 2.5$ eV. It almost diminishes when $\hbar\omega$ lies in the range 0.5 to 1.3 eV, which is mainly due to the large gap between the 0.3 and 1.2 eV in the band structure (Fig. S2). In the dc limit ($\omega = 0$), the real part of σ_{ac} is essentially identical to σ_{xy} (right panel of Fig. 3a). In the *p*-doping state (negative relative chemical potential), one always sees a large ac Hall of $\sim 2 e^2/h$ at $\hbar\omega = 0.4$ eV, which disappears in the *n*-doping state. The real and imaginary parts of σ_{ac} in the intrinsic state (chemical potential at the Fermi level) are also shown in Supplementary Information (Fig. S3).

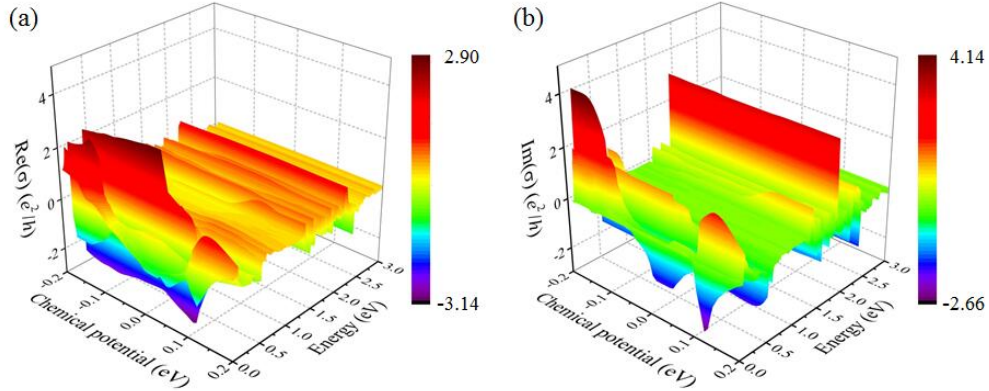


Figure 4. Real and imaginary parts of the optical conductivity σ_{xy} with respect to photonic energy and chemical potential.

In order to further study the QAH effects of RuI_3 , we calculate the in-plane strain effect on magnetic exchange and the global band gap (Fig. 5). We find that, with the nontrivial band topology preserved, a compressive strain increases the bulk band gap, while the tensile strain decreases it. The nontrivial band gap becomes 21 meV when a 2% in-plane compression is applied. On the other hand, the exchange parameter J increases monotonically as the lattice expands. Thus, one can apply an appropriate in-plane strain to achieve an optimal working temperature.

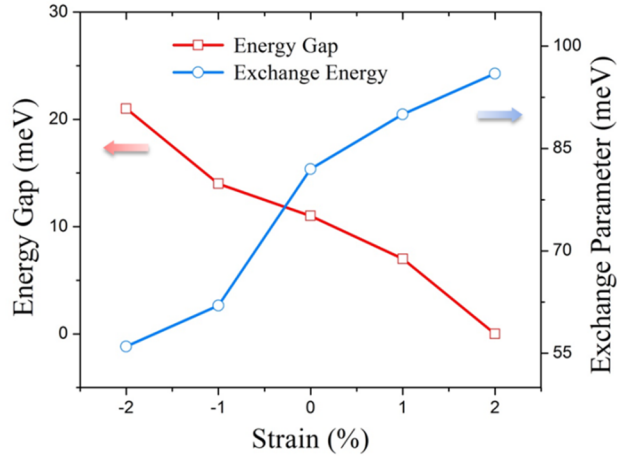


Figure 5. Nontrivial bulk energy gap and magnetic exchange parameter J as functions of biaxial in-plane strain.

Besides RuI₃ monolayer we also investigate similar RuCl₃ and RuBr₃ monolayers. Our GGA and GGA+*U* calculations show that their exchange energies are very small and sensitive to the effective *U* values. This suggests that the ground states of RuCl₃ and RuBr₃ monolayers lie at the border between FM and AFM configurations. Hence, in order to achieve robust FM states, one needs to explicitly apply a weak external magnetic field or a small in-plane strain. Nevertheless, we also find similar topological features in FM RuCl₃ and RuBr₃ monolayers. The calculated band structures (without and with SOC) of FM RuCl₃ and RuBr₃ monolayers show similar behavior as the RuI₃ monolayer (Fig. S3). When the SOC is absent, we again find Dirac point at the *K* point in the spin down channel. When the SOC is included, the degeneracy of Dirac point is lifted and a nontrivial energy gap opens at the *K* point. This shows the same nontrivial band topology as in RuI₃ monolayer. However, in both cases, the conduction band drops below the Fermi level around the Γ point, and the valence band lies above the Fermi level around the *M* point. This suggests that both of these materials would show semi-metallic features (with nonzero anomalous Hall conductance) rather than QAH insulating. In spite of this, due to our previous results for RuI₃ monolayer, one still would observe chiral dissipation-less edge state in their corresponding nanoribbons, and expect that the QAH insulating state can be achieved by applying a weak external magnetic field and/or small in-plane strain.

In summary, based on first-principles DFT calculations, we predict that 2D RuI₃ monolayer is a robust intrinsic FM QAH insulator. This material could be synthesized in experiments and the TM atoms are uniformly distributed. The Curie temperature is estimated to be \sim 360 K, higher than most of the 2D FM thin films studied hitherto. Without including SOC interaction, a Dirac point in the spin down channel appears at the Fermi level, which is contributed by Ru-*d* orbitals and protected by crystal symmetry of Ru sublattice. The mechanism of such Dirac point has been understood by considering the ligand field effect, hybridization, and magnetic exchange field interactions. Once the

SOC is introduced, the symmetry protected Dirac point opens a band gap and the system becomes a QAH insulator with a global band gap of 11 meV. Thus, the topologically nontrivial band gap is robust against perturbations that retain its crystal symmetry. The nontrivial band topology and intrinsic QAH effect are demonstrated by calculating its Berry curvature, Chern number, and chiral edge state. In-plane strain effects are also discussed which are expected to play a role in tailoring both the band gap and the Curie temperature. We look forward to experimental verifications of the QAH effects in the ruthenium halide family.

Computational Methods

Our first-principles calculations are based on spin polarized density functional theory (DFT) with generalized gradient approximation (GGA) for exchange-correlation potential given by Perdew, Burke, and Ernzerhof (PBE)³⁶, as implemented in the Vienna *Ab initio* Simulation Package (VASP)³⁷. A vacuum space of 20 Å along the *z* direction was adopted to model the 2D system. The projector augmented wave (PAW) method³⁸ was used to treat the core electrons, while the valence electrons were represented using planewave basis set. The planewave cutoff energy was set to be 500 eV, and the first Brillouin zone was sampled using a Γ -centered (12×12×1) Monkhorst-Pack grid³⁹. The convergence criteria for energy and force were set to be 10⁻⁵ eV and 0.01 eV/Å, respectively. The SOC was included in the self-consistent calculations. In order to integrate Berry curvature, a much denser *k*-mesh of (120×120×1) was adopted. To verify the GGA results, we also repeated our calculations using the GGA+*U* method⁴⁰, with effective Hubbard *U* value of 0.5, 1.0, and 1.5 eV for Ru-*d* electrons. Very similar results have been obtained (Table S2).

Acknowledgement.

E.K. is supported by the NSFC (11374160, 51522206, 11574151), by NSF of Jiangsu

Province (BK20130031), by PAPD, the Fundamental Research Funds for the Central Universities (No.30915011203), and by New Century Excellent Talents in University (NCET-12-0628). C.H. and E.K. acknowledge the support from the Shanghai Supercomputer Centre. P.J. acknowledges support by the U.S. Department of Energy, Office of Basic Energy Sciences, Division of Materials Sciences and Engineering under Award # DE-FG02-96ER45579. J.Z. and P.J. acknowledge the resources of the National Energy Research Scientific Computing Center supported by the Office of Science of the U.S. Department of Energy under Contract no. DE-AC02-05CH11231. C.H. acknowledges the China Scholarship Council (CSC) for sponsoring his visit to Virginia Commonwealth University (VCU) where this work was conducted.

Author contributions

C.H. and J. Z. contributed equally to this work. C.H. and E. K. conceived the concept. C.H. and J. Z. performed the calculations. All authors analyzed the results, discussed the results and wrote the manuscript.

Additional information

Supplementary information is available in the online version of the paper. Reprints and permissions information is available online at www.nature.com/reprints.

Correspondence and requests for materials should be addressed to J. Z., J. P., or E. K.

Competing financial interests

The authors declare no competing financial interests.

Supplementary Information. AIMD simulation results, different magnetic coupling configurations, comparison of MLWF and DFT calculated band structure, and band structures of RuCl_3 and RuBr_3 .

References:

- (1) Moore, J. E. The birth of topological insulators. *Nature* **464**, 194-198 (2010).
- (2) Hasan, M. Z. & Kane, C. L. Colloquium: Topological insulators. *Rev. Mod. Phys.* **82**, 3045-3067 (2010).
- (3) Qi, X.-L. & Zhang, S.-C. The quantum spin Hall effect and topological insulators. *Phys. Today* **63**, 33-38 (2010).
- (4) Checkelsky, J. G., Yoshimi, R., Tsukazaki, A., Takahashi, K. S., Kozuka, Y., Falson, J., Kawasaki, M. & Tokura, Y. Trajectory of the anomalous Hall effect towards the quantized state in a ferromagnetic topological insulator. *Nat. Phys.* **10**, 731-736 (2014).
- (5) Weng, H., Yu, R., Hu, X., Dai, X. & Fang, Z. Quantum anomalous Hall effect and related topological electronic states. *Adv. Phys.* **64**, 227-282 (2015).
- (6) Liu, C.-X., Zhang, S.-C. & Qi, X.-L. The Quantum Anomalous Hall Effect: Theory and Experiment. *Annu. Rev. Condens. Matter Phys.* **7**, 301-321 (2016).
- (7) Haldane, F. D. M. Model for a Quantum Hall Effect without Landau Levels: Condensed-Matter Realization of the “Parity Anomaly”. *Phys. Rev. Lett.* **61**, 2015-2018 (1988).
- (8) Yu, R., Zhang, W., Zhang, H. J., Zhang, S. C., Dai, X. & Fang, Z. Quantized Anomalous Hall Effect in Magnetic Topological Insulators. *Science* **329**, 61-64 (2010).
- (9) Xu, G., Wang, J., Felser, C., Qi, X.-L. & Zhang, S.-C. Quantum Anomalous Hall Effect in Magnetic Insulator Heterostructure. *Nano Lett.* **15**, 2019-2023 (2015).
- (10) Zhang, H., Lazo, C., Blügel, S., Heinze, S. & Mokrousov, Y. Electrically Tunable Quantum Anomalous Hall Effect in Graphene Decorated by 5d Transition-Metal Adatoms. *Phys. Rev. Lett.* **108**, 056802 (2012).
- (11) Wang, Z. F., Liu, Z. & Liu, F. Quantum Anomalous Hall Effect in 2D Organic

Topological Insulators. *Phys. Rev. Lett.* **110**, 196801 (2013).

(12) Dong, L., Kim, Y., Er, D., Rappe, A. M. & Shenoy, V. B. Two-Dimensional π -Conjugated Covalent-Organic Frameworks as Quantum Anomalous Hall Topological Insulators. *Phys. Rev. Lett.* **116**, 096601 (2016).

(13) Wu, S.-C., Shan, G. & Yan, B. Prediction of Near-Room-Temperature Quantum Anomalous Hall Effect on Honeycomb Materials. *Phys. Rev. Lett.* **113**, 256401 (2014).

(14) Chang, C.-Z. *et al.* Experimental Observation of the Quantum Anomalous Hall Effect in a Magnetic Topological Insulator. *Science* **340**, 167-170 (2013).

(15) Kou, X., Guo, S.-T., Fan, Y., Pan, L., Lang, M., Jiang, Y., Shao, Q., Nie, T., Murata, K., Tang, J., Wang, Y., He, L., Lee, T.-K., Lee, W.-L. & Wang, K. L. Scale-Invariant Quantum Anomalous Hall Effect in Magnetic Topological Insulators beyond the Two-Dimensional Limit. *Phys. Rev. Lett.* **113**, 137201 (2014).

(16) Chang, C.-Z., Zhao, W., Kim, D., Zhang, Y. H., Assaf, B. A., Heiman, D., Zhang, S.-C., Liu, C., Chan, M. H. W. & Moodera, J. S. High-precision realization of robust quantum anomalous Hall state in a hard ferromagnetic topological insulator. *Nat. Mater.* **14**, 473-477 (2015).

(17) Zhang, D. M. *et al.* Interplay between ferromagnetism, surface states, and quantum corrections in a magnetically doped topological insulator. *Phys. Rev. B* **86**, 205127 (2012).

(18) Zhang, J. S. *et al.* Topology-driven magnetic quantum phase transition in topological insulators. *Science* **339**, 1582-1586 (2013).

(19) Troyanov, S. I. & Snigireva, E. M. X-ray-diffraction Study of Phase-transition in Alpha-TiCl₃. *Zh. Neorg. Khim.* **36**, 1117-1123 (1991).

(20) Bengel, H., Cantow, H. J., Magonov, S. N., Hillebrechtb, H., Thieleb, G., Liangc, W. & Whangbo, M. H. Tip-force Induced Surface Corrugation in Layered Transition-metal Trichlorides MCl₃ (M = Ru, Mo, Rh, Ir). *Sur. Sci.* **343**, 95-103

(1995).

(21) Banerjee, A. *et al.* Proximate Kitaev quantum spin liquid behavior in a honeycomb magnet. *Nat. Mat.* doi:10.1038/nmat4604

(22) Nicolosi, V., Chhowalla, M., Kanatzidis, M. G., Strano, M. S. & Coleman, J. N. Liquid Exfoliation of Layered Materials. *Science* **340**, 1226419 (2013).

(23) Liu, J., Sun, Q., Kawazoe, Y. & Jena, P. Exfoliating biocompatible ferromagnetic Cr-trihalide monolayers. *Phys. Chem. Chem. Phys.* **18**, 8777-8784 (2016).

(24) Zhang, W.-B., Qu, Q., Zhu, P. & Lam, C.-H. Robust intrinsic ferromagnetism and half semiconductivity in stable two-dimensional single-layer chromium trihalides. *J. Mater. Chem. C* **3**, 12457 (2015).

(25) Zhou, Y., Lu, H., Zu, X. & Gao, F. Evidencing the existence of exciting half-metallicity in two-dimensional $TiCl_3$ and VCl_3 sheets. *Sci. Rep.* **6**, 19407 (2016).

(26) Kim, H.-S., Shankar, V. V., Catuneanu, A. & Kee, H.-Y. Kitaev magnetism in honeycomb $RuCl_3$ with intermediate spin-orbit coupling. *Phys. Rev. B* **91**, 241110 (2015).

(27) Kan, M., Wang, B., Lee, Y. H. & Sun, Q. A density functional theory study of the tunable structure, magnetism and metal–insulator phase transition in VS_2 monolayers induced by in-plane biaxial strain. *Nano. Res.* **8**, 1348-1356 (2015).

(28) Li, X., Wu, X. & Yang, J. Half-Metallicity in $MnPSe_3$ Exfoliated Nanosheet with Carrier Doping. *J. Am. Chem. Soc.* **136**, 11065-11069 (2014).

(29) Zhou, J. & Sun, Q. Magnetism of Phthalocyanine-Based Organometallic Single Porous Sheet. *J. Am. Chem. Soc.* **133**, 15113-15119 (2011).

(30) Yao, Y. G. & Fang, Z. Sign Changes of Intrinsic Spin Hall Effect in Semiconductors and Simple Metals: First-Principles Calculations. *Phys. Rev. Lett.* **95**, 156601 (2005).

(31) Guo, G. Y., Yao, Y. G. & Niu, Q. *Ab initio* Calculation of the Intrinsic Spin Hall Effect in Semiconductors. *Phys. Rev. Lett.* **94**, 226601 (2005).

(32) Wang, Q.-Z., Liu, X., Zhang, H.-J., Samarth, N., Zhang, S.-C. & Liu, C.-X. Quantum Anomalous Hall Effect in Magnetically Doped InAs/GaSb Quantum Wells. *Phys. Rev. Lett.* **113**, 147201 (2014).

(33) Qiao, Z., Ren, W., Chen, H., Bellaiche, L., Zhang, Z., MacDonald A. H. & Niu, Q. Quantum Anomalous Hall Effect in Graphene Proximity Coupled to an Antiferromagnetic Insulator. *Phys. Rev. Lett.* **112**, 116404 (2014).

(34) Marzari, N., Mostofi, A. A., Yates, J. R., Souza, I. & Vanderbilt, D. Maximally localized Wannier functions: Theory and applications. *Rev. Mod. Phys.* **84**, 1419 (2012).

(35) Mostofi, A. A., Yates, J. R., Lee, Y.-S., Souza, I., Vanderbilt, D. & Marzari, N. Wannier90: A tool for obtaining maximally-localised Wannier functions. *Comput. Phys. Commun.* **178**, 685 (2008).

(36) Perdew, J. P., Burke, K. & Ernzerhof, M. Generalized Gradient Approximation Made Simple. *Phys. Rev. Lett.* **77**, 3865 (1996).

(37) Kresse, G. & Hafner, J. *Ab initio* molecular dynamics for liquid metals. *Phys. Rev. B* **47**, 558-561 (1993).

(38) Blöchl, P. E. Projector augmented-wave method. *Phys. Rev. B* **50**, 17953 (1994).

(39) Monkhorst, H. J. & Pack, J. D. Special points for Brillouin-zone integrations. *Phys. Rev. B*, **13**, 5188-5192 (1976).

(40) Dudarev, S., Botton, G., Savrasov, Y., Humphreys, C. & Sutton, A. *Phys. Rev. B* **57**, 1505 (1998).